White Rose Research Online
eprints@whiterose.ac.uk
https://eprints.whiterose.ac.uk
Universities of Leeds, Sheffield and York

Deposited via The University of Leeds.

White Rose Research Online URL for this paper:
https://eprints.whiterose.ac.uk/id/eprint/128509/

Version: Accepted Version

Article:

Garufo, A, Carluccio, G, Freeman, JR et al. (2018) Norton Equivalent Circuit for Pulsed Photoconductive Antennas - Part II: Experimental Validation. IEEE Transactions on Antennas and Propagation, 66 (4). pp. 1646-1659. ISSN: 0018-926X

https://doi.org/10.1109/TAP.2018.2800704

(c) 2018, IEEE. Personal use of this material is permitted. Permission from IEEE must be obtained for all other uses, in any current or future media, including reprinting/republishing this material for advertising or promotional purposes, creating new collective works, for resale or redistribution to servers or lists, or reuse of any copyrighted component of this work in other works.

Reuse

Items deposited in White Rose Research Online are protected by copyright, with all rights reserved unless indicated otherwise. They may be downloaded and/or printed for private study, or other acts as permitted by national copyright laws. The publisher or other rights holders may allow further reproduction and re-use of the full text version. This is indicated by the licence information on the White Rose Research Online record for the item.

Takedown

If you consider content in White Rose Research Online to be in breach of UK law, please notify us by emailing eprints@whiterose.ac.uk including the URL of the record and the reason for the withdrawal request.

UNIVERSITY OF LEEDS
University of Sheffield
UNIVERSITY of York

Norton Equivalent Circuit for Pulsed Photoconductive Antennas – Part II: Experimental Validation

Alessandro Garufo, *Member, IEEE*, Giorgio Carluccio, Joshua R. Freeman, David R. Bacon, Nuria Llombart, *Senior Member, IEEE*, Edmund H. Linfield, Alexander G. Davies, and Andrea Neto, *Fellow, IEEE*

***Abstract*—This second part of two papers sequence presents the experimental validation of the Norton equivalent circuit model for pulsed photoconductive antennas provided in the first paper of the sequence. To this goal different prototypes of photoconductive antenna sources have been manufactured and assembled. The average powers radiated and their pertinent energy spectral densities have been measured. In order to obtain a validation of the original equivalent circuit proposed, an auxiliary electromagnetic analysis of the complete setup, including the quasi-optical link for the signals from the antenna feeds to the detectors had to be developed. By using the combined theoretical model (circuit and quasi-optics), an excellent agreement is achieved between the measured power and the power estimated. This agreement fully validates the circuit model, which can now be used to design new photoconductive antennas, including optical and electrical features of the semiconductor materials, as well as the details of the antenna gaps and the purely quasi-optical components.**

***Index Terms*—Equivalent circuit, photoconductivity, THz photoconductive antenna, THz radiated power, THz source, THz technology, THz measurement.**

I. INTRODUCTION

MAny researchers have characterized the performances of photoconductive antennas (PCAs) [1]–[9] using measurements in the past. However, in most cases the analysis of the results was presented without having a characterization of the Quasi-Optical (QO) channel, which typically includes the lens antenna (PCA plus lens), a chain of reflectors, and the detector. Such channels are typically extremely inefficient, causing the power detected to be smaller, in the order of tenths, than the one generated by the PCA. The lack of such quasi-optical characterization for the channel typically renders impossible to calculate how much power was actually generated by the source, giving rise to the wide spread use of arbitrary units. In Part I of this two papers sequence [10], some of the authors have presented a model to estimate the power radiated by a pulsed PCA source, based on its optical, electrical, and geometrical operating parameters. In this second part of the sequence a measurement setup is discussed, prototypes of standard PCAs are presented, and the average powers generated by the PCAs and their pertinent spectra have been measured. In order to deconvolve the impact of the quasi-optical path, a dedicated accurate electromagnetic model for the channel has been developed, so that a power complete budget from the source to the detector has been characterized and completely validated by measurements.

The most commonly used geometries for PCAs have been chosen for the analysis: H-dipole, bow-tie, and logarithmic spiral antennas. One prototype of each geometry has been manufactured, maintaining for all these sources the same geometrical gap dimensions, the semiconductor material, and the same optical and bias excitations. The power measurement setup was composed of an optical system that guides and collimates the laser beam, a QO channel, and a power detector. Two power detectors have been used (and the specific features of both have been retained in the analysis): a cryo-cooled bolometer with a high sensitivity and fast response [11], and a calorimetric power meter with a lower sensitivity and a slower response [12]. The bolometer has been calibrated and the power meter has been characterized with the same commercially available source [13]. Excellent agreement between the detectors gives high confidence on the accuracy of the power measurements. Moreover, spectral measurements have been carried out by using a different setup where an Electro-Optic (EO) crystal paired with balanced photodiodes was employed to measure the time-domain signal and energy spectral density.

The estimation of the power budget of each antenna has been made by computing the radiated energy spectral density by using the circuit model in Part I of this sequence, and then propagating coherently the associated waves to the detectors. A good agreement between the measurements and the theoretical results is found, within the limited uncertainties of the measurement setup and material properties. The comparative analysis of the performances of the different PCAs provides clear evidence of the major impact of the antenna properties of the sources. The relevant detected energy spectral density of the devices is significantly affected by the direction, within the lens, in which the relevant generated THz power is radiated

---

Manuscript received Month DD, YYYY; revised Month DD YYYY. First published Month DD, YYYY; current version published Month DD, YYYY. This work was supported by the European Research Council Starting Grants ERC-2011-StG Grant AAATSI, No. 278794, and ERC-2014-StG Grant LAA-THz-CC, No. 639749.

A. Garufo, G. Carluccio, N. Llombart, and A. Neto are with the Microelectronics Department of the Electrical Engineering, Mathemathics and Computer Science Faculty, Delft University of Technology, Mekelweg 4, 2628 CD Delft, The Netherlands (e-mail: a.garufo@tudelft.nl, g.carluccio@tudelft.nl, n.llombartjuan@tudelft.nl, a.neto@tudelft.nl).

J. R. Freeman, D. R. Bacon, E. H. Linfield, and A. G. Davies are with Institute of Microwaves and Photonics of the School of Electronic and Electrical Engineering, University of Leeds, Woodhouse Lane, LS29JT, Leeds, United Kingdom (e-mail: j.r.freeman@leeds.ac.uk, el09d2b@leeds.ac.uk, e.h.linfield@leeds.ac.uk, g.davies@leeds.ac.uk)

Color versions of one or more of the figures in this paper are available online at http://ieeexplore.ieee.org.

Digital Object Identifier XX.XXXX/TAP.XXXX.XXXXXXXX.

[14].

The present validation of the novel equivalent circuit allows the vast range of wideband microwave engineering tools, that have been developed mostly for analyzing detectors in radiometric domains, to be extended to PCA antenna design. The results of this paper can be expected to open the way for more standard engineering optimization of wideband coherent THz sources [15].

The paper is organized as follow: Section II describes the manufactured photoconductive antenna prototypes; Section III describes the measurement setups used for the power measurements; Section IV presents the electromagnetic model which characterizes the measurement setups in terms of efficiency; Section V discusses the estimation of the radiated and detected energy spectral density and the relevant average power for the different PCA prototypes; Section VI and Section VII present the power and energy spectral density measurement results and the relevant comparisons against the ones predicted by theoretical model, respectively. Finally, Section VIII discusses some concluding remarks.

II. PCA PROTOTYPES DESCRIPTION

Three different photoconductive antenna geometries have been manufactured, in order to measure their radiated average power and compare it with the results derived by the equivalent circuit model discussed in [10]. The chosen antenna geometries are a H-dipole, a bow-tie, and a logarithmic spiral antenna, shown in Fig. 1. The H-dipole and the bow-tie have standard design features. The logarithmic spiral has been designed according to [16] with the limitation of designing a gap of length $W_y = 10\,\mu\text{m}$. The geometrical features of the antennas are listed in the caption of Fig. 1.

The three different devices were fabricated on the same semiconductor wafer. The layers structure of the chip is shown in Fig. 2(a). It is composed of a $2\,\mu\text{m}$ thick LT-GaAs layer grown on a $400\,\text{nm}$ thick AlGaAs layer with 0.75% of Al content; itself grown on a GaAs buffer layer of thickness $200\,\text{nm}$ placed on a $525\,\mu\text{m}$ thick SI-GaAs wafer. The relative permittivity of the chip layers is about $\varepsilon_{\text{GaAs}} = 13$.

For most devices, the samples were fabricated without annealing [17], [18]. The lack of such process in the fabrication of the material results in low values of dark resistivity of the LT-GaAs and, subsequently, high values of dark current in the devices, as it is shown in Fig. 3.

For comparison, an additional device, a bow-tie with identical geometrical details, has been manufactured on an annealed LT-GaAs wafer. Because of the annealing process such device presents a much lower dark current than the corresponding not annealed device, as it is also shown in Fig. 3. It is noted that such annealing process has been optimized [17], in order to do not affect consistently the carriers lifetime, and consequently the radiated energy at higher frequencies ($f > 1\,\text{THz}$).

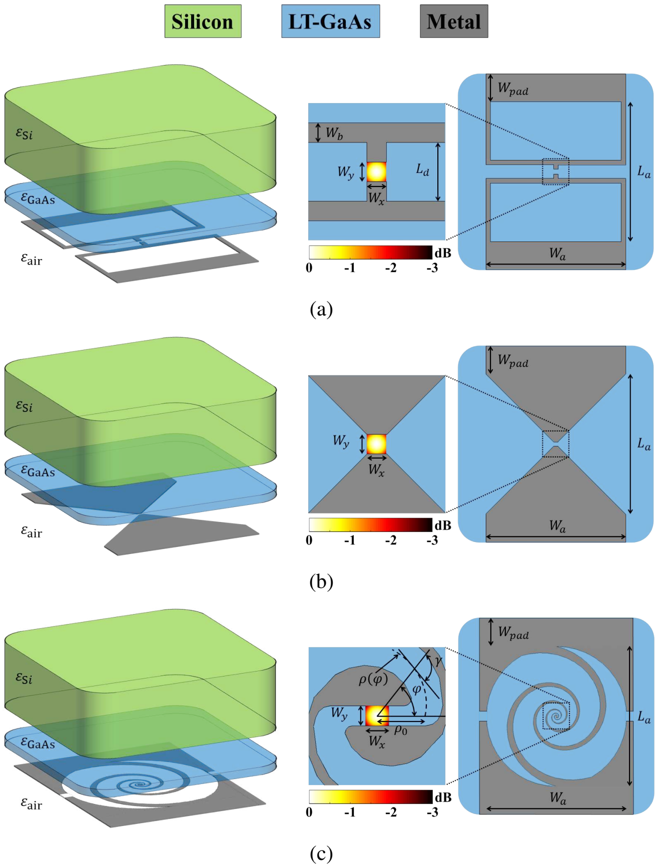

(a)

(b)

(c)

Figure 1. PCA prototype geometries under analysis. The blue slab represents the chip of photoconductive material; the green thick slab depicts the silicon lens; whereas the antenna metallizations are depicted in grey. a) H-dipole antenna: gap size $W_x = W_y = 10\,\mu\text{m}$, dipole length $L_d = 30\,\mu\text{m}$ and bias lines width $W_b = 10\,\mu\text{m}$. b) Bow-tie antenna: gap size $W_x = W_y = 10\,\mu\text{m}$ and tapering angle 90°. c) Logarithmic spiral antenna: $\rho(\varphi) = \rho_0 e^{a\varphi}$ with $\varphi \in [0, 2\pi N]$, starting radius $\rho_0 = 23\,\mu\text{m}$, curvature angle $\gamma = 76.5°$, winding number $N = 2.6$, tapering angle $\delta = 150°$ and gap width $W_y = 10\,\mu\text{m}$. All three geometries have the same overall sizes and the bias pads width: $L_a = 2\,\text{mm}$, $W_a = 2\,\text{mm}$, and $W_{pad} = 0.5\,\text{mm}$. In the zoom of the gap of each antenna, it is shown the normalized laser power density distributions used in the experiment, $D_{laser} = 16\,\mu\text{m}$, for the evaluation of the energy spectral density in Fig. 10(a).

Each antenna chip was mounted on a Printed Circuit Board (PCB), gluing the bias pads on the two bias lines printed on the PCB by means a conductive silver glue. On the opposite side of the patterned antenna metalization, a silicon lens [19] with relative permittivity $\varepsilon_{\text{Si}} = 11.9$, diameter $D_{lens} = 10\,\text{mm}$, and extension length $E_{lens} = 0.16R_{lens}$ is placed. The extension length was chosen to get an overall extension length, including the thickness of the chip, close to the ideal hyperhemispherical extension of the lens $0.29R_{lens}$. The choice of the hyperhemispherical lens has been dictated by the requirement of a constant directivity over the entire operative bandwidth, in order to match a reflectors system. The gluing of the lens has been made on two posts placed on the sides of the PCB aperture and slightly lower than the chip, in order to minimize any possible gap between the chip and the lens interface due to the glue itself, Fig. 2(b). The alignment procedure has ensured an accuracy of about $20\,\mu\text{m}$ on the placement of the lens with respect to the antenna center. The gluing procedure of the chip and the lens was performed in clean room (SRON, see Acknoledgment), in order to minimize the possible presence of dust particles. To provide the biasing voltage to the PCB lines, a SMA connector was soldered at the end of the bias lines. The fabricated PCA prototypes are shown in Fig. 2(c).

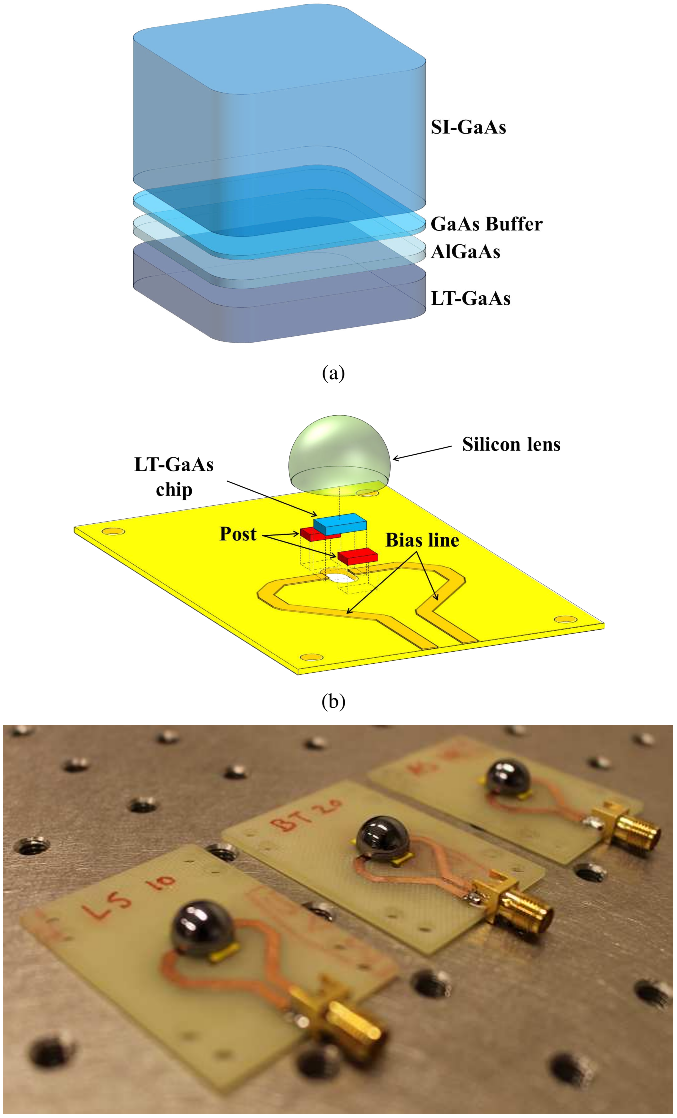

(a)

(b)

(c)

Figure 2. Photoconductive antenna prototypes and their components: a) layered structure of the LT-GaAs chip used for the PCA prototypes, b) structure of the PCB used for biasing the PCAs, c) photoconductive antenna prototypes.

III. MEASUREMENT SETUP

The power measurements have been carried out using the two different measurements setups shown in Fig. 4. Both setups were composed of the same optical and QO systems: the first one (not shown in Fig. 4) was used to drive and focus the laser excitation $\mathbf{s}_{laser}\left(\mathbf{r};t\right)$ on the antennas' gap; whereas, the second one was used to focus the THz radiation emitted by the PCAs onto the detector. The only differences between the setups were the two different power detectors used.

A Gaussian envelope pulsed laser was used for the experiment. The laser presents the following features: carrier frequency $f_{laser} = 375\,\mathrm{THz}$ (central wavelenght $\lambda_{laser} = 800\,\mathrm{nm}$), half-power pulse duration $\tau_p = 100\,\mathrm{fs}$, and pulse repetition rate $f_p = 80\,\mathrm{MHz}$.

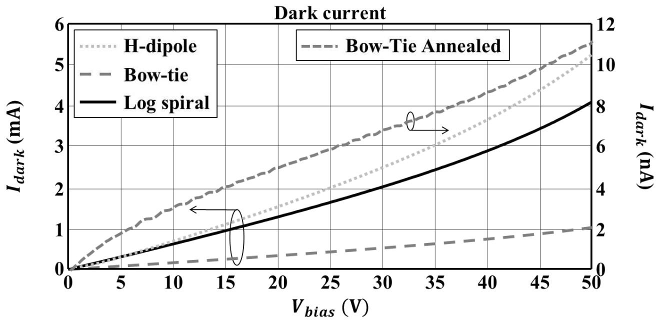

Figure 3. Measured dark current of PCA prototypes.

The optical path of the laser beam ends with a $2.5\,\mathrm{cm}$ diameter achromatic lens with a focal length of $4.5\,\mathrm{cm}$. The lens was used to focus the laser beam on the photoconductor gap of the PCA under test. The position of the focusing lens has been chosen so that the focal point of the focusing lens have been matched with the nominal position of the antenna gap. Since the uniform illumination of the entire surface of the focusing lens with the laser was not achieved, the actual numerical aperture of the lens was reduced. For this reason the width of the laser beam has been measured. Fig. 5 shows the laser beam diameter at $-3\,\mathrm{dB}$ measured by means of the knife-edge technique on a longitudinal range of $1\,\mathrm{mm}$ and centered at the focal point of the focusing lens. The minimum laser beam diameter ($-3\,\mathrm{dB}$ power level with respect to the maximum) obtained by such lens was about $D_{laser} = 16\,\mu\mathrm{m}$, which ensured a nearly uniform illumination of the PCAs' gap, once the antenna gap was aligned to the laser beam at the focal point of the lens. The QO system was composed of two 90° off-axis parabolic reflectors. The features of the system are listed in the caption of Fig. 4. The position of the emitter with respect to the first reflector has been chosen in such a way to match the phase center of the hyperhemispherical lens antenna, placed behind the antenna plane $\Delta_{pc}^{PCA} = 16\,\mathrm{mm}$, with the focal point of the parabolic reflector, $d_{t,1} = f_{R1} - \Delta_{pc}^{PCA} = 85.6\,\mathrm{mm}$ as it shown in the insets of Fig. 4(a)-4(b). The first detector, used to perform the alignment procedure, was a cryo-cooled bolometer [11]. The bolometer was operating at a temperature of $4\,\mathrm{K}$ with a lock-in frequency of $167\,\mathrm{Hz}$, to reach a sensitivity of about $-35\,\mathrm{dB}\mu\mathrm{W}$. A Winston cone, with f-number $f_{\#} = 3.5$, mounted on the cold plate, collected the power coming from the QO system. The aperture of the bolometer was at a distance $d_{2,r} = 80\,\mathrm{mm}$ from the center of the second reflector of the QO system. The calibration of the bolometer was performed by using an autocalibrating absolute power meter [20] and a commercial photomixer [13], in order to derive the calibration factor to be used for converting the voltage readout of the lock-in amplifier in the measured power. The bolometer was used to perform the alignment of the antenna gap with the laser beam, as well as to measure the radiated average power of the PCA prototypes.

The second detector, used for the measurement, was a room temperature calorimetric power meter [12], where the sensor is coupled with the QO system via a conical horn antenna

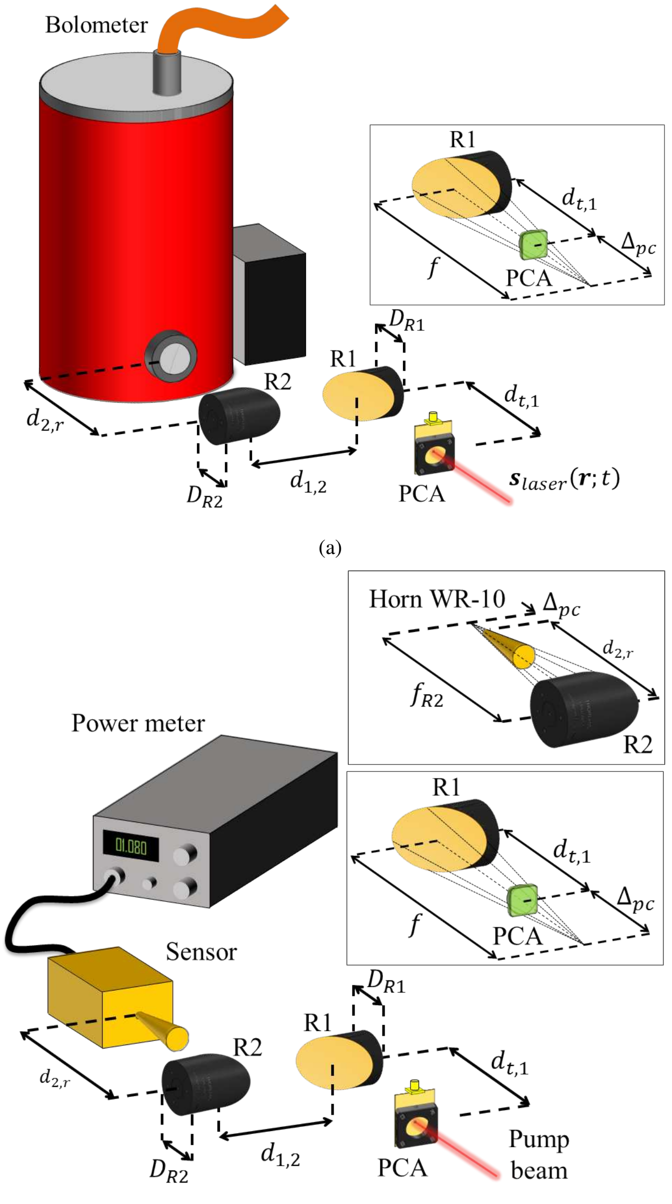

(a)

(b)

Figure 4. Measurement setups used to measure the power radiated by the photoconductive antenna prototypes, the optical system is not depicted in the figures. The geometrical features of the setups are: reflectors diameter $D_{R1} = D_{R2} = 50.8\,\mathrm{mm}$: reflectors f-number $f_{\#1} = f_{\#2} = 2$; distance emitter-first reflector $d_{t,1} = 85.6\,\mathrm{mm}$; distance reflectors $d_{1,2} = 95\,\mathrm{mm}$. a) Bolometer based setup used for the alignment procedure. The distance second reflector-bolometer aperture was $d_{2,r} = 80\,\mathrm{mm}$. b) Power meter based setup. The distance second reflector-horn antenna was $d_{2,r} = 91.6\,\mathrm{mm}$.

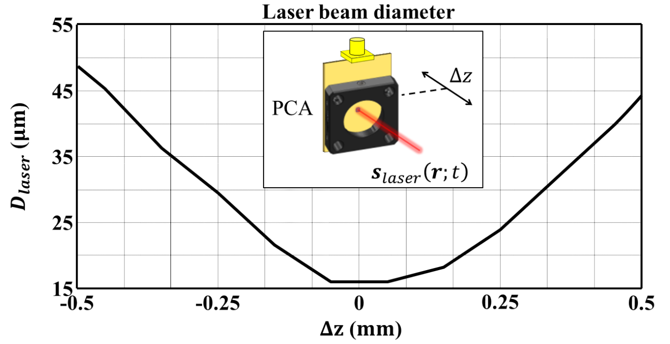

Figure 5. Measured laser beam diameter at $-3\,\mathrm{dB}$ around the focal point of the laser focusing lens.

Figure 6. Measurement setup used for the alignment of the photoconductive antenna and the laser beam.

WR-10. Performing an OFF-ON-OFF measurement procedure [12], [21], such detector can reach a sensitivity of $-5\,\mathrm{dB}\mu\mathrm{W}$. The characterization of such detector was also performed by using a commercial photomixer with known output power [13] and it is shown in detail in Appendix A. The conical horn WR-10 [12] connected to the sensor, with aperture diameter $D_{horn} = 16.3\,\mathrm{mm}$ and length $L_{horn} = 35.5\,\mathrm{mm}$, was located in such way that the phase center of the fundamental mode of the horn antenna, placed behind the horn mouth connected to the waveguide at a distance $\Delta_{pc}^{Horn} = 10\,\mathrm{mm}$, was at the focal point of the second reflector of the QO system, $d_{2,r} = f_{R2} - \Delta_{pc}^{Horn} = 91.6\,\mathrm{mm}$ as it is shown in the inset in Fig. 4(b). For both the setups a $5\,\mathrm{mm}$ thick filter screen of expanded Polytetrafluoroethylene (ePTFE) was placed between the second reflector and the detector, in order to screen possible thermal InfraRed (IR) power generated by the source (this screen is not depicted in Fig. 4). A picture of the measurement setup with the bolometer is shown in Fig. 6.

IV. ANALYSIS OF THE MEASUREMENT SETUP

For sake of compactness, only the analysis of the power meter setup is discussed in this section, the same analysis can be conducted for the bolometer setup.

The characterization of the measurements setup has been performed in terms of efficiency of all the setup stages on the radiated pulsed bandwidth. Such characterization has been calculated in time-harmonic regime, and it has been used to perform the energy spectral densities analysis, in order to estimate the dispersion introduced by the measurement setup.

The three antenna chip geometries, mentioned in Section II, have been simulated by the EM commercial software [22], assuming the chip structure to radiate between free space and a semi-infinite dense dielectric medium, which simulates the presence of the dielectric silicon lens [14]. The simulated radiation patterns of the antennas in the semi-infinite silicon medium have been used to compute the fields radiated by the dielectric lens of the prototypes via a Physical Optic (PO) approach [23], [24].

By using the simulated radiation patterns from the lens, the power P_l radiated by the lens has been computed as the integral of the radiated power density distribution outside the lens. The radiation efficiency of lens antenna η_l have been evaluated as the ratio between the power P_l and the power P_{source} generated at the input port of the antenna at each frequency:

$$\eta_l\left(\omega\right) = \frac{P_l\left(\omega\right)}{P_{source}\left(\omega\right)} \tag{1}$$

η_l takes into account the front-to-back losses; the dielectric losses of the silicon according to [25], and the reflection losses at the lens interface [23]. The metalizations ohmic losses have not been considered since they are negligible. The lens antenna efficiency of each prototypes is shown in Fig. 7(a). The logarithmic spiral and the bow-tie lens feeds present a quite constant efficiency behaviour over the operative bandwidth. The spiral lens antenna is slightly more efficient than the bow-tie lens antenna because of the broadside radiation of the spiral feed inside the lens [16], as it is shown in Fig. 8(e)-8(f), which decreases the reflection losses with respect to the bow-tie antenna, which indeed illuminates consistently the lateral part of the lens [14], see Fig. 8(c)-8(d). More critical is the radiation efficiency of the H-dipole lens antenna. The long bias lines contribute strongly to the radiation at the lower frequencies, illuminating the lens mainly in the lateral part and resulting in very high reflection losses [14], as it is shown in Fig. 8(a)-8(b).

In order to analyze the behaviour of the QO system when it was fed by the PCA prototypes, the electromagnetic behaviour of the reflectors system has been simulated by means of a PO approach implemented in the commercial software [26]. The field used to illuminate the first reflector was the one estimated by the PO lens simulations. The power P_{rs}, captured by the last reflector, has been evaluated as the integral of the radiated power density distribution of the electromagnetic field impinging on the surface of the last reflector of the reflectors system. The reflectors system efficiency η_{rs} is defined as the ratio between the power P_{rs} and the power P_l at each frequency:

$$\eta_{rs}\left(\omega\right) = \frac{P_{rs}\left(\omega\right)}{P_l\left(\omega\right)} \tag{2}$$

η_{rs} takes into account the spillover losses of the reflectors chain. The reflectors system efficiency for each prototype illumination is shown in Fig. 7(b). The hyperhemispherical lens geometry, discussed in Section II, has been chosen in such a way to reduce the angular variation of the secondary patterns over the entire bandwidth. However, only the logarithmic spiral lens antenna presents a nearly constant directivity over the considered bandwidth [27]. Then the antennas were placed at the position where their phase center and the focus of the first reflector were matched. The choice of this location for the lens antennas also permits the reflector surface to be fed with a nearly constant phase radiation pattern. The highest spillover efficiency is from the reflectors system fed by the logarithmic spiral lens antenna over the entire bandwidth due to the better lens illumination. The broadside field radiated by the spiral lens feed illuminates more homogeneously the upper part of the lens [16], resulting in more directive beams radiated by the lens, as it is shown in Fig. 9(e)-9(f). The lower spillover efficiency provided by the reflectors system fed by the bow-tie is due the consistent illumination of the lateral part of the lens [14], which indeed results in broader radiated beams in one plane with respect to an ideal uniform lens illumination, as in Fig. 9(c)-9(d). Concerning the H-dipole feeding, since it illuminates the lateral part of the lens at the lower frequencies [14], the patterns radiated by the lens are not well focused, thus spreading the radiated energy outside the reflector area, as it is shown in Fig. 9(a). Consequently the reflectors system suffers from high spillover losses. At the higher frequencies, the radiation of the small dipole becomes more relevant than the one that comes from the long bias line, thus providing a more homogeneous illumination of the upper part of the lens similar to the bow-tie, as a consequence the radiation patterns become more directive, as in Fig. 9(b), resulting in a reduction in the spillover and an increase in efficiency.

Finally, the coupling between the beam emerging from the last reflector and the detector has been simulated by a Method of Moment (MoM) implemented in the commercial software [26]. The input electromagnetic field to the MoM was the one calculated by the simulation of the reflectors system. The power P_d, impinging on the sensor at the end of the waveguide inside the detector, has been evaluated by integrating the power density distribution of the electromagnetic field traveling inside an infinite waveguide. The detector efficiency for quantifying the coupling between the field focused by the reflectors system and the detector has been defined as the ratio between the power P_d and the power P_{rs} at each frequency, namely:

$$\eta_d\left(\omega\right) = \frac{P_d\left(\omega\right)}{P_{rs}\left(\omega\right)} \tag{3}$$

η_d takes into account the coupling losses between the reflectors system, the conical horn antenna, and the waveguide inside the detector. The detector efficiency of each prototypes is shown in Fig. 7(c). The position of the detector has been chosen in such a way that the phase center of the fundamental mode of the conical horn antenna was matched with the focus of the second reflector, in order to maximize the coupling between the reflectors system and the detector. The reflectors system fed by the bow-tie and the logarithmic spiral PCA present high coupling efficiencies with the detector. On the contrary, the reflectors system fed by the H-dipole presents a lower coupling efficiency, especially at the lower frequencies, since the reflectors system suffers of the poor focusing of the beam

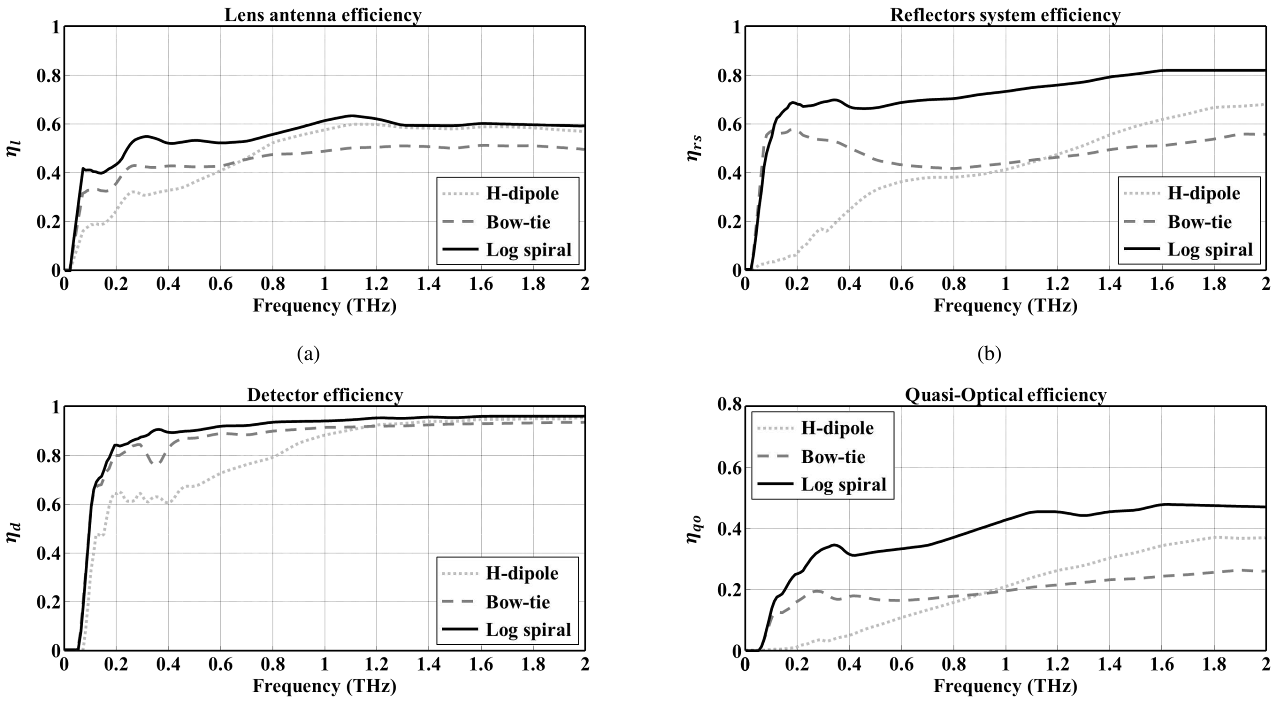

(a) (b)

(c) (d)

Figure 7. Simulated efficiencies of the measurement setup: a) lens antenna efficiency η_l, b) reflectors system efficiency η_{rs}, c) detector efficiency η_d, and d) quasi-optical efficiency η_{qo} of the measurements setup.

into the detector. This is again due to the poor illumination of the reflectors system provided by the radiation pattern of the lens fed by the H-dipole antenna. Since part of the power meter consists of a WR-10 waveguide, one can note that the detector does not absorb the power below the cut-off frequency of the fundamental mode of the waveguide $f_{c_{1,0}} = 59\,\mathrm{GHz}$. Moreover, because of the very large operative bandwidth, high-order modes are excited in the waveguide at the higher frequencies.

The product of the three efficiencies discussed above determines the efficiency η_{qo} of the entire QO channel at each frequency:

$$\eta_{qo}(\omega) = \eta_l(\omega)\,\eta_{rs}(\omega)\,\eta_d(\omega) \tag{4}$$

The QO efficiency η_{qo} is shown in Fig. 7(d). The measurement setup fed by the bow-tie presents a nearly flat total efficiency over the entire operative band. The logarithmic spiral presents a better total efficiency which increases with the frequency. The higher efficiency provided by the logarithmic spiral feed with respect to the bow-tie feed is due to the better illumination of the lens provided by the pattern radiated by the spiral.

V. ESTIMATION OF THE RADIATED AND MEASURED ENERGY SPECTRAL DENSITIES AND POWERS

The radiated energy spectral density E_s radiated by each PCA prototypes are calculated by using the Norton equivalent circuit described in [10]:

$$E_s(\omega) = Z_a(\omega)\left|\frac{Z_g(\omega)}{Z_a(\omega)+Z_g(\omega)}\right|^2 |I_g(\omega)|^2 \tag{5}$$

where:

$$\begin{aligned} I_g(\omega) = {} & \eta(W_x, W_y, W_z, A_{laser}) \cdot \\ & \cdot \frac{A_{laser}}{W_y^2} e\,\mu\,H(\omega)\,\tilde{S}(\omega)\,V_{bias} \end{aligned} \tag{6}$$

$$\begin{aligned} Z_g(\omega) = {} & \Bigg[\eta(W_x, W_y, W_z, A_{laser}) \cdot \\ & \cdot \frac{A_{laser}}{W_y^2} \frac{e\,\mu}{\tau_\sigma} H(\omega=0)\,\tilde{S}(\omega=0)\Bigg]^{-1} \end{aligned} \tag{7}$$

are the equivalent Norton generator current spectrum and impedance, respectively, which model the photoconductive source, and $Z_a(\omega)$ is the antenna impedance. In (6)–(7), the following parameters are defined as in [10]: the laser absorption efficiency η; the gap dimensions (W_x, W_y, W_z); the area of the spatial distribution of the Poynting vector of the laser beam A_{laser}; the electron charge e; the carriers transient mobility μ; the frequency response to the laser excitation of the photoconductor material $H(\omega)$; the spectrum of the time-varying envelope of the laser pulse $\tilde{S}(\omega)$; the bias voltage V_{bias}; and the time duration of the pulsed photoconductivity τ_σ.

For the experiment we consider a bias voltage $V_{bias} = 40\,\mathrm{V}$ and a laser average power $\bar{P}_{laser} = 30\,\mathrm{mW}$. The laser power was assumed to be focused on the photoconductive gap according to laser beam measurement performed in the measurements setup. Therefore, for the calculation of the energy spectral densities, the laser beam diameter has been considered to be the minimum size measured, $D_{laser} = 16\,\mu\mathrm{m}$, as it shows in

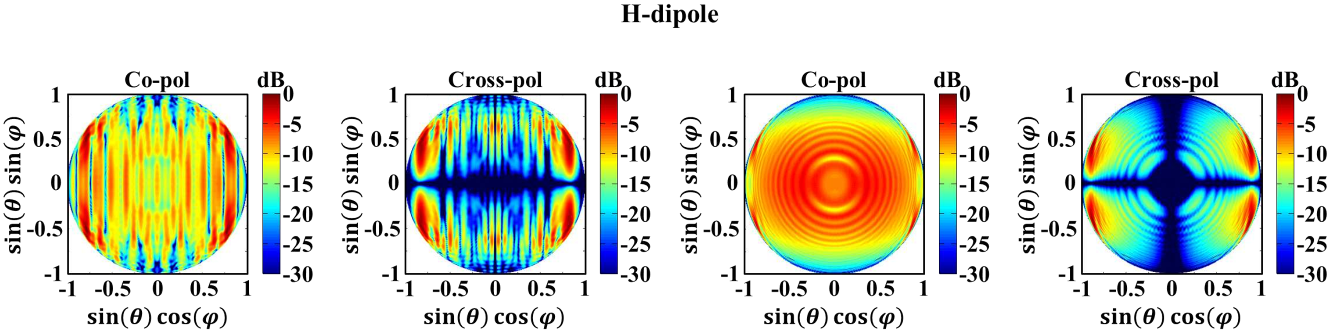

(a) $f = 0.5\,\mathrm{THz}$

(b) $f = 1.5\,\mathrm{THz}$

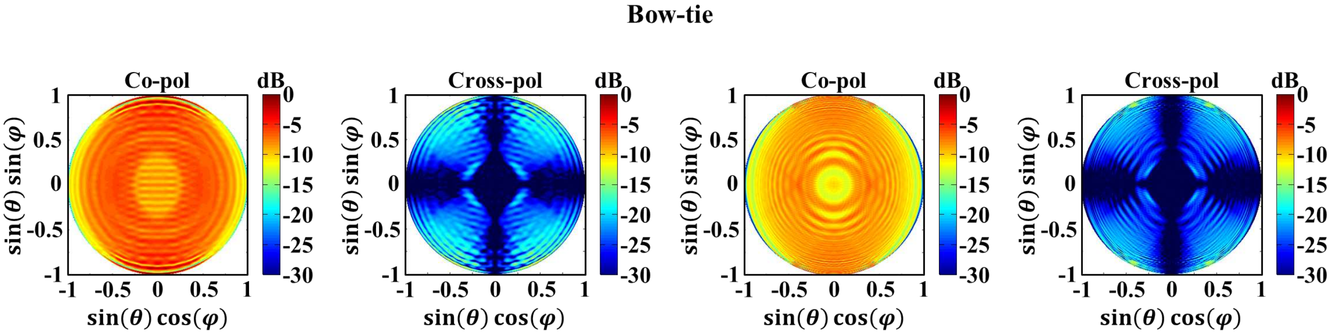

(c) $f = 0.5\,\mathrm{THz}$

(d) $f = 1.5\,\mathrm{THz}$

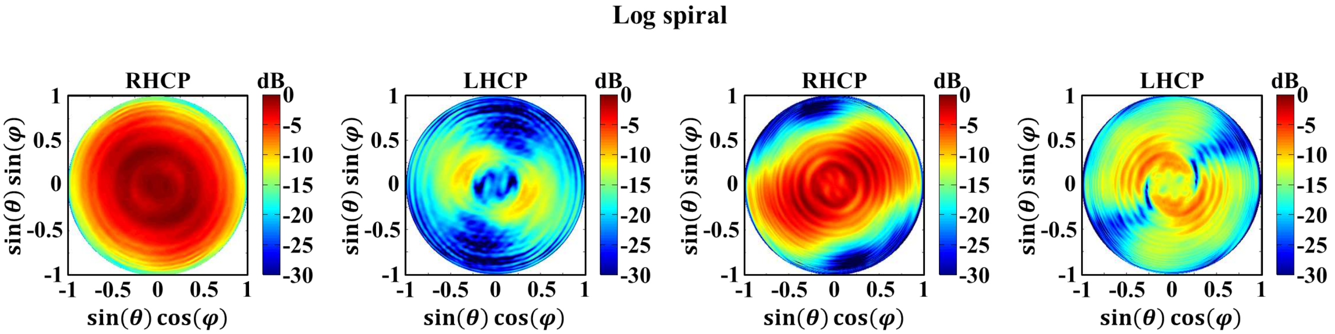

(e) $f = 0.5\,\mathrm{THz}$

(f) $f = 1.5\,\mathrm{THz}$

Figure 8. 2D plots of the simulated radiation patterns inside the dielectric lens (primary fields) of the lens antenna feeds described in Section II: a)-b) H-dipole, c)-d) bow-tie, and e)-f) logarithmic spiral.

Fig. 5. Referring to the insets in Fig. 1, the sizes of the gap area illuminated by the laser beam for the three geometries have been considered as follows: $W_x = W_y = 10\,\mu\mathrm{m}$ for the H-dipole and the bow-tie antenna, whereas $W_x = 12\,\mu\mathrm{m}$ and $W_y = 10\,\mu\mathrm{m}$ for the logarithmic spiral antenna due to the geometry of its gap.

The absorption coefficient and carrier lifetime of the LT-GaAs layers used for the modeling of the PCA prototypes are $\alpha = 10^6\,\mathrm{m}^{-1}$ and $\tau = 0.3\,\mathrm{ps}$, respectively. The carriers transient mobility of the not annealed LT-GaAs was considered to be $\mu = 60\,\mathrm{cm}^2/\mathrm{Vs}$, in agreement to what discussed in [18], [28], [31]. Such low values of carriers transient mobility is due to the fact that the material was manufactured without being annealed, thus resulting in a low dark resistivity of the material [17], [18]. This implies a high dark current (Fig. 3) and, subsequently, a high working temperature, which affects the carriers transient mobility [18], [28]–[31]. Whereas, the carriers transient mobility of the annealed LT-GaAs was considered to be $\mu = 240\,\mathrm{cm}^2/\mathrm{Vs}$, in agreement with the discussion in [32]–[34].

The real part of the energy spectral densities radiated by the antennas are shown in Fig. 10(a). They have similar behaviour at the higher frequencies. Significant differences can be appreciated at the lower frequencies, where the antennas present different resonant behaviours due to the finite extents of the different structures.

Having the complete characterization of the measurement setup in terms of efficiency at each frequency, one can estimate the received energy spectral density E_m, starting from the generated energy spectral density of the antenna E_s as:

$$E_m(\omega) = \eta_{qo}(\omega)\, E_s(\omega) \tag{8}$$

The estimation of the real part of the measured energy spectral

H-dipole

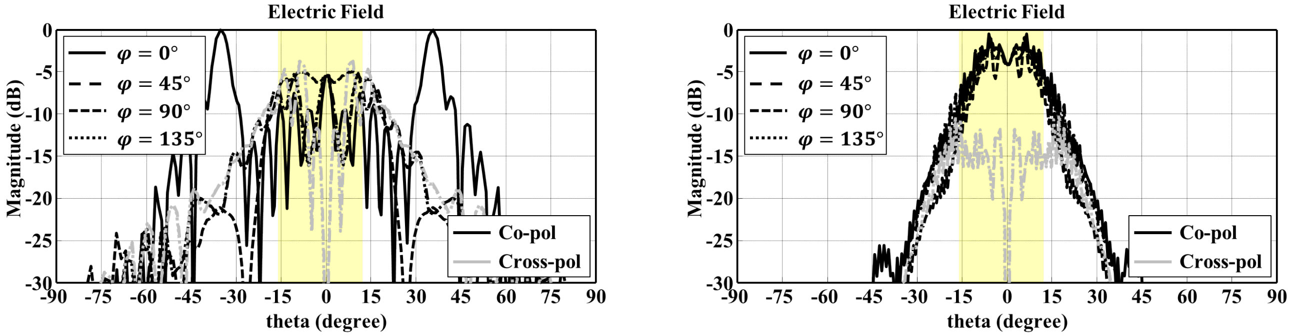

(a) $f = 0.5\,\mathrm{THz}$

(b) $f = 1.5\,\mathrm{THz}$

Bow-tie

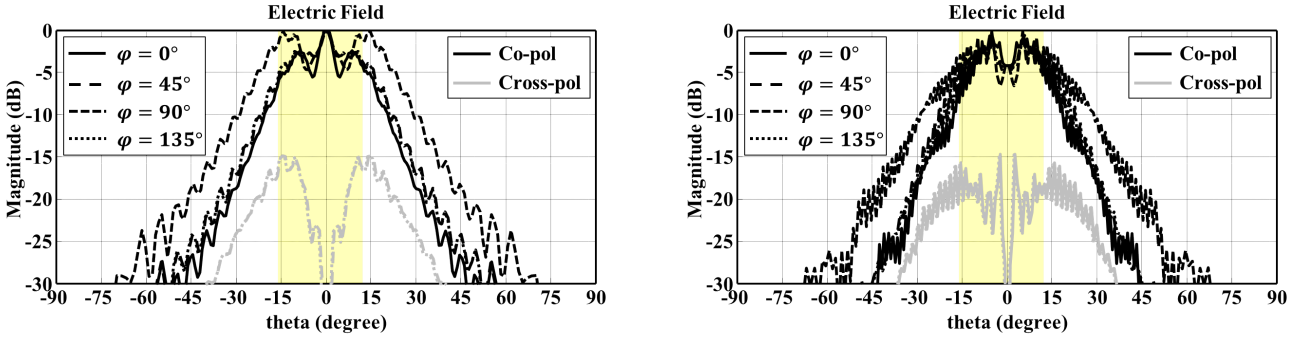

(c) $f = 0.5\,\mathrm{THz}$

(d) $f = 1.5\,\mathrm{THz}$

Log spiral

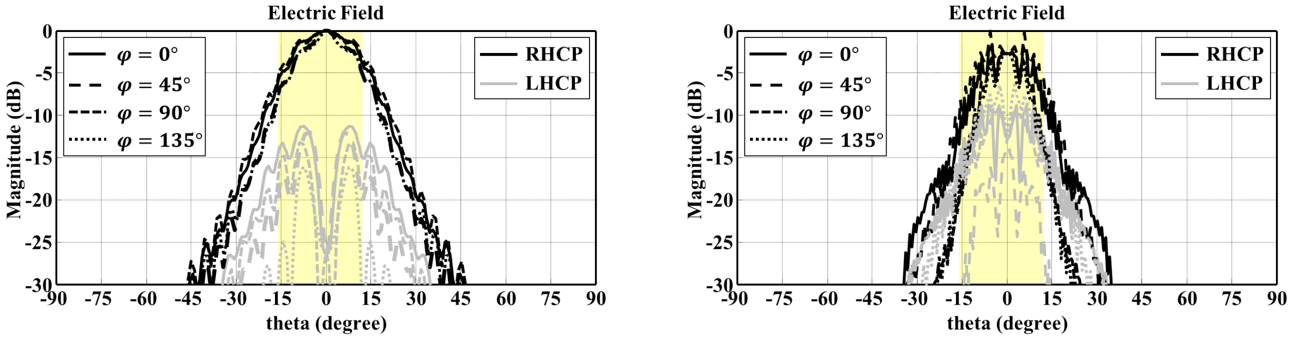

(e) $f = 0.5\,\mathrm{THz}$

(f) $f = 1.5\,\mathrm{THz}$

Figure 9. Simulated radiation patterns outside the dielectric lens (secondary fields) of the lens antennas described in Section II: a)-b) H-dipole, c)-d) bow-tie, and e)-f) logarithmic spiral. The shaded yellow region represents the angular range subtended by the area of the first reflector of the reflectors chain in the measurement system described in Section III

.

density is shown in Fig. 10(b). One can note that the different radiation features of the antennas, and the relevant interaction with the measurement system setup, affect the estimation of measured energy spectral density in different ways. The spectra of the logarithmic spiral and bow-tie are similar, showing only a different attenuation over the bandwidth, due to the higher lens reflection losses and spillover losses of the bow-tie antenna with respect to the logarithmic spiral. On the contrary, the estimation of the measured spectrum of the H-dipole shows a strong attenuation of the components at the lower frequencies.

The single pulse radiated (E_{source}) and measured (E_{meas}) energy can be calculated by integrating the relevant energy spectral density, respectively, i.e.:

$$E_{source,meas} = \frac{1}{2\pi} \int_{-\infty}^{+\infty} E_{s,m}\left(\omega\right) \mathrm{d}\omega \tag{9}$$

Since the PCA radiates pulses periodically with a period $T_p =$

Table I
ESTIMATED AND MEASURED AVERAGE POWER OF THE PHOTOCONDUCTIVE ANTENNA PROTOTYPES UNDER ANALYSIS.

	Generator Impedance Z_g	**Estimated Power**			**Measured Power**	
		$\bar{P}_{available}$	$\bar{P}_{source}$	$\bar{P}_{meas}$	**Bolometer**	**Power meter**
H-dipole not annealed	$2.25\,\mathrm{k\Omega}$	$44.6\,\mu$W	$5.8\,\mu$W	$0.6\,\mu$W	$0.4\,\mu$W	$0.5\,\mu$W
Bow-tie not annealed	$2.25\,\mathrm{k\Omega}$	$44.6\,\mu$W	$5.0\,\mu$W	$0.8\,\mu$W	$0.8\,\mu$W	$0.7\,\mu$W
Log spiral not annealed	$1.9\,\mathrm{k\Omega}$	$51.7\,\mu$W	$5.2\,\mu$W	$1.4\,\mu$W	$1.1\,\mu$W	$1.2\,\mu$W
Bow-tie annealed	$564\,\Omega$	$178.3\,\mu$W	$67.7\,\mu$W	$11.2\,\mu$W	$10.3\,\mu$W	—

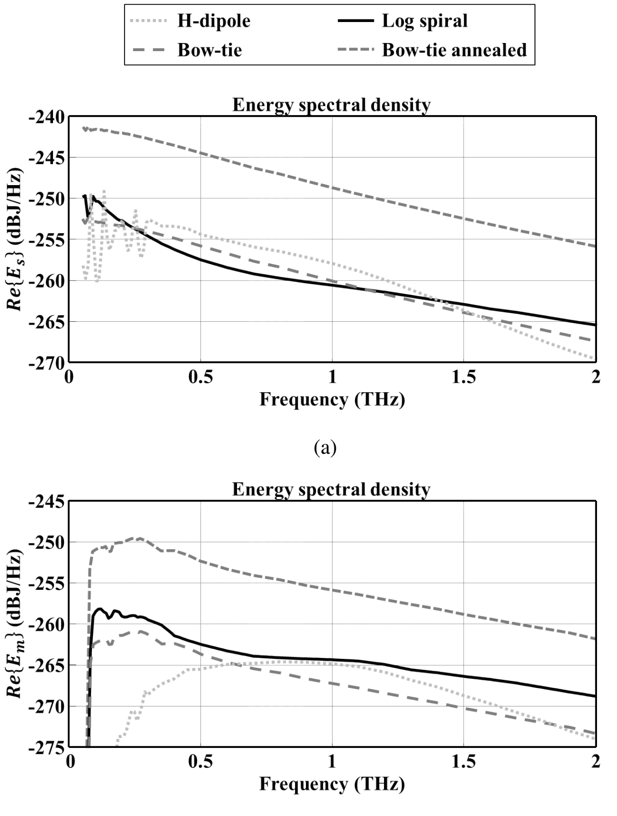

(a)

(b)

Figure 10. Simulated energy spectral densities of the PCA prototypes: a) generated energy spectral densities E_s; b) received energy spectral densities E_m.

$1/f_p$, where f_p is the repetition rate of the laser, the average power radiated and measured can be calculated, respectively, as:

$$\bar{P}_{source,meas} = \frac{E_{source,meas}}{T_p} \tag{10}$$

As it can be seen in Table I (fourth column), similar values of average power radiated $\bar{P}_{source}$ have been estimated for each antenna geometry with the not annealed LT-GaAs substrate. Comparing such values with the average power radiated by the PCA with the annealed material, it is worth noting that the not annealed devices radiate much less power than the annealed one. This significant difference is due to the dependency of the free carriers transient mobility with respect to the working temperature of the photoconductor substrate [30]. Indeed, in dark regime (i.e., in absence of optical pump), the not annealed material presents a higher dark current than the annealed one, as shown in Fig. 3. As a consequence, the dark resistivity of the annealed substrate in the gap is much higher than the not annealed one [17]. The dark current is mainly due to the hopping conduction mechanism [35], [17], [28], related to carriers in intraband gap and not in the conduction band. Due to the high density of As defects in the GaAs lattice, the dark current is high, leading to a high working temperature, because of the Joule heating. On the contrary, the annealing creates As clusters, thus increasing the distances between the defects, and reducing the dark current by hopping conduction [35], [17], [28], and the relevant working temperature. Instead, the transient current, induced by the optical pump, is related to the free carriers in the conduction band. The working temperature of the semiconductor affects the free carriers transient mobility, which decreases as the working temperature of the material increases [30]. Therefore, the resulting transient conductivity is lower for the not annealed material than the annealed one. As a result, the equivalent generator of the annealed material presents a higher current and a higher conductance than the not annealed one, leading to a lower generator impedance according to (6) and (7). Therefore, a better impedance matching between source and antenna is achieved with the annealed device, as can be noted by comparing the generator impedance listed in the second column of Table I and the simulated antenna impedances shown in Fig. 11. This leads to a significant enhancement of the radiated power for the annealed device. However, in the presented experiment, the generator impedance value of the annealed material is still too high to perform an ideal impedance matching with any antenna.

The radiated energy spectral density E_s can be related to the energy spectral density E_s^{max} associated to the maximum available energy provided to the antenna, if the antenna load matches the equivalent generator impedance, as defined by (13) in [10]:

$$E_s(\omega) = \eta_m(\omega)\, E_s^{max}(\omega) \tag{11}$$

The maximum available average power $\bar{P}_{available}$ can thus be estimated by integrating the relevant energy spectral density:

$$\bar{P}_{available} = \frac{1}{2\pi T_p} \int_{-\infty}^{+\infty} E_s^{max}(\omega)\, \mathrm{d}\omega \tag{12}$$

The maximum available average power provided by the an-

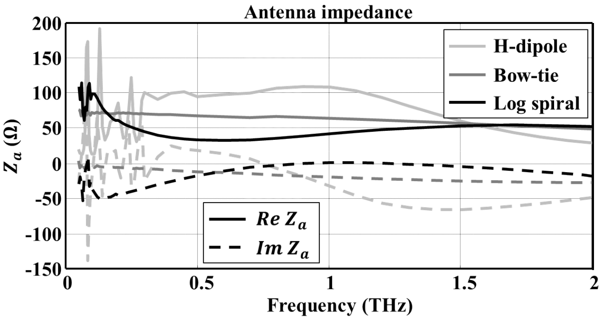

Figure 11. Simulated input impedances of the antenna geometries under analysis.

tennas under the working condition of the experiment are listed in the third column of Table I. The results show clearly that the power $\bar{P}_{source}$ radiated by the antennas is much lower than the available one $\bar{P}_{available}$, due to the fact that the photoconductor sources are mismatched with the antenna loads.

The values of the measured power $\bar{P}_{meas}$ of the three PCA prototypes (evaluated by the procedure mentioned above) are listed in the fifth column of Table I. Comparing the not annealed devices first, as expected, the logarithmic spiral provides the highest value of detected power, meanwhile the H-dipole provides the lowest one. However, all the antennas provide a poor total efficiency. Only the 28%, 16%, and 10% of the power $\bar{P}_{source}$ radiated by the spiral, the bow-tie, and the H-dipole, respectively, is expected to be measured.

VI. MEASURED POWER OF THE PCA PROTOTYPES

The power measurement procedure was composed by two phases, by using the two detectors described in Section III. The cryo-cooled bolometer was used to perform the alignment of the antennas with the laser beam, because of the faster response of the bolometer with respect to the one of the power meter. Once that the optimal alignment of the antenna with the laser and the QO system was achieved, ensuring to have maximized the read out of the lock-in amplifier, the value of the measurement was acquired. After, the bolometer was replaced by the power meter sensor, and the measurement was acquired again, performing the OFF-ON-OFF measurement procedure. The antennas under test were measured using the laser average power and bias voltage mentioned in Section V. The devices were biased with a voltage square wave with frequency $f_{bias} = 7\,\mathrm{kHz}$, and a duty cycle of 50%. A chopper was placed in the optical path before the focusing lens and provided the reference frequency of the lock-in amplifier. Similar values of average power have been measured by both detectors for each prototypes and they are listed in the last two columns of Table I (since during the power measurements of the annealed device the VDI power meter was not available, the relevant measure is not present in the table). In order to have a fair comparison between the values measured with both detectors, the readout of the power meter has been divided by the duty cycle factor of the bias voltage signal. The values of the measured powers of all the devices find a good agreement with the values of the detected power $\bar{P}_{meas}$ evaluated by using the proposed equivalent circuit.

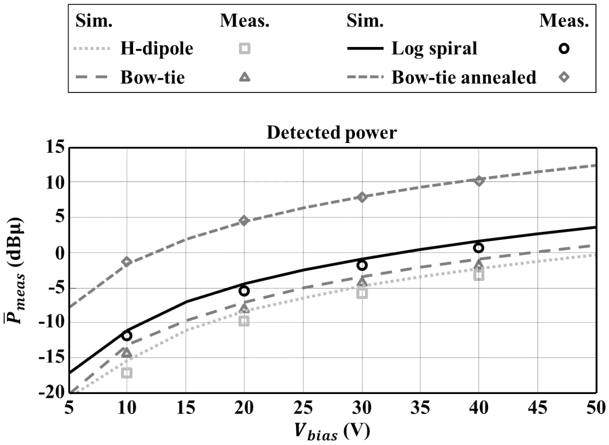

Figure 12. Measured power and power $\bar{P}_{meas}$ estimated by using the equivalent circuit versus the bias voltage applied of the PCAs.

Furthermore, a comparison between the power $\bar{P}_{meas}$ estimated and measured by varying the applied bias voltage is also shown in Fig. 12. In this case the values of measured power refer to measurements conducted with the bolometer, since the sensitivity of the power meter was not enough to detect such low power levels emitted by the not annealed devices with low values of bias voltage V_{bias}. Again, the prediction of the model is in very good agreement with the measurement results.

VII. MEASURED SPECTRA OF THE PCA PROTOTYPES

The spectra of the PCA prototypes have also been measured by using the Electro-Optic (EO) sampling technique [36]. A $2\,\mathrm{mm}$ thick ZnTe crystal paired with balanced photodiodes was used. The signal was recorded using a lock-in amplifier, referenced to the emitter bias modulation frequency. The measurements have been carried out in a purged environment with dry air, in order to eliminate any water absorption. According to the EO sampling technique, the radiated THz pulse is measured, by estimating the differential current flowing in the photodiodes. Such current is proportional to the amplitude of the pulsed electric field impinging on the crystal at the sampling instant [37]. Since the current pulse measured by the photodiodes is proportional to the THz electric field illuminating the crystal, it is possible to compare the Fourier Transform (FT) of the squared amplitude of the measured current pulse against the energy spectral density E_r captured by the last reflector of the reflectors system evaluated by using the electromagnetic model proposed in this paper, i.e.,

$$E_r(\omega) = \eta_l(\omega)\,\eta_{rs}(\omega)\,E_s(\omega) \tag{13}$$

The normalized amplitude spectra of the measured pulse of the different PCA prototypes and the relevant estimated real part of the energy spectral densities E_r are shown in Fig. 13.

It is worth noting that the measured spectra are also affected by the response of the EO crystal excited by the THz pulse, which is not known both in amplitude and in phase. Hence, the

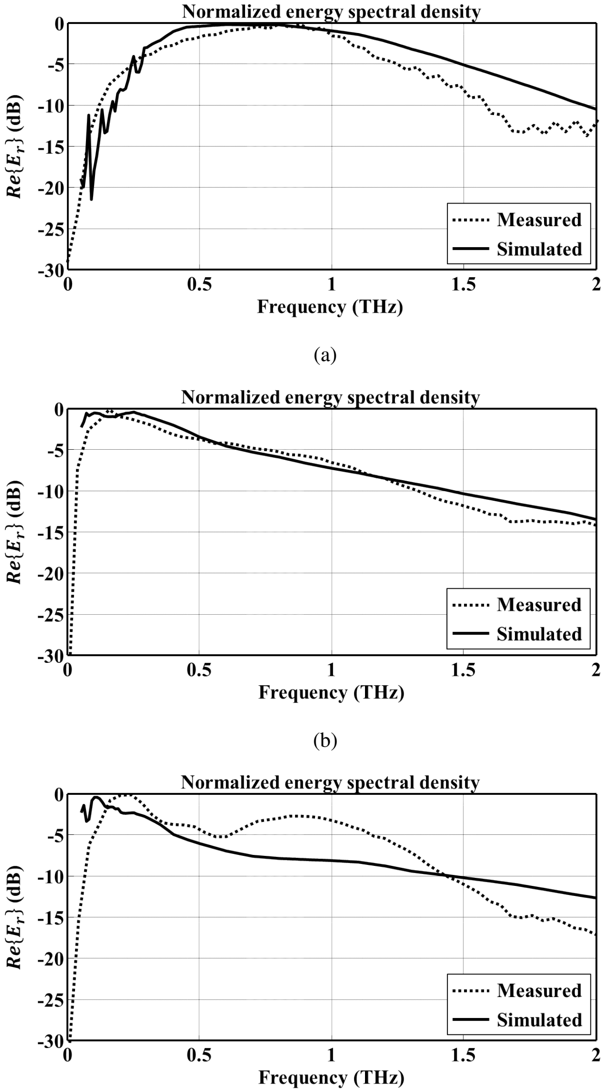

(a)

(b)

(c)

Figure 13. Comparison between the energy spectral densities, obtained by the measured pulses radiated by the PCA protoypes, and the simulated energy spectral densities radiated by the reflectors system evaluated by using the equivalent circuit: a) H-dipole, b) bow-tie, and c) logarithmic spiral.

comparison is only qualitative. On the contrary, the estimated spectra E_r do not take into account such response. One can note a fair agreement between the simulated and measured spectra, especially for the H-dipole (Fig. 13(a)) and the bow-tie antenna (Fig. 13(b)). For the logarithmic spiral antenna the behaviour of the curves is slightly different (Fig. 13(c)). Indeed, the EO crystal is well known to have an anisotropic behaviour [37], and this significantly affects the measurement of the field radiated by the logarithmic spiral antenna, whose radiated field is elliptically polarized. Such anisotropic behaviour can be appreciated in Fig. 14, which shows the ratio between two spectrum measurements obtained by two orthogonal orientations of the EO crystal.

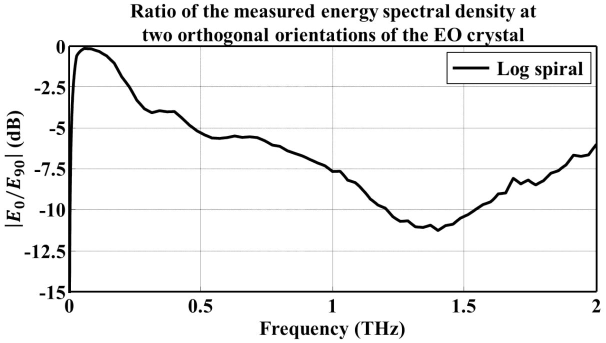

Figure 14. Ratio of two measured energy spectral densities amplitudes obtained by two orthogonal orientations of the EO crystal.

VIII. CONCLUSION

In this work, an electromagnetic model for the measurement of THz power radiated on a large bandwidth is proposed. The measurement system setup and the relevant coupling to the PCA radiated field is described in terms of its efficiency over the operative bandwidth. The measurements of the power radiated by three different PCA prototypes have been discussed. Such measurements have been compared against the power evaluated by using the proposed electromagnetic model. The results of the analysis have also been used to validate the equivalent circuit model introduced in [10].

The analysis shows clearly the different behaviours of the energy spectral densities radiated by the PCAs and coupled to the measurement system setup, thus giving a clear picture about the reasons of different values of power measured by the detector for different antenna geometries.

The values of power, evaluated by using the proposed electromagnetic model, find a good agreement with the values of the measured power. Furthermore, the comparison between the measured spectra and the estimated spectra are in fair agreement. Such results also provide a solid validation of the equivalent circuit model proposed in [10], which can be effectively used to design PCAs.

ACKNOWLEDGMENT

The authors would like to thank SRON (Netherlands Institute for Space Research) for having provided its technical support for the assembly of the prototypes components.

The authors would like to thank the anonymous reviewers for their useful comments and their careful review of this paper.

APPENDIX A
CHARACTERIZATION OF THE POWER METER

The room temperature calorimetric power meter (VDI Erickson PM5 [12]) has been characterized before using it for the measurements. The characterization has been performed comparing the emitted power of a commercial photomixer (Toptica Terascan 1550 [13]) measured with the power detector [12] and the reference power provided by the manufacturer [38]. The measurements have been performed by coupling the photomixer to the detector with a QO system (the same as used to characterize it by the manufacturer [38], [39]) and scanning the frequency of the source over its bandwidth (i.e. $0.1\,\mathrm{THz} - 1\,\mathrm{THz}$). Because of the low level of power at the higher frequency, the measurements have been acquired by the OFF-ON-OFF measurement procedure suggested by the manufacturer of the detector [12], [21].

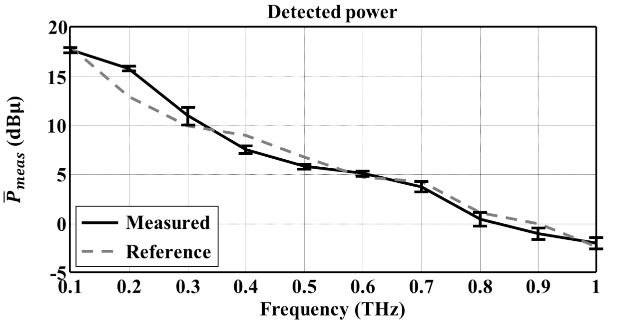

Figure 15. Comparison between the power measured by the detector [12] and the reference curve of the power provided by the manufacturer [13], [38].

The comparison between the average of ten power measurements at each frequency by using the power meter (solid black line) and the reference power curve provided by the manufacturer is shown in Fig. 15. The error bars in the plot show the range as large as six standard deviation of the measurements at each frequency. Since the reference power was measured with a different detector [39], in order to have a fair comparison, the measurements have been corrected for the coupling efficiency η_d of the detector [12]. The QO channel [38]–[40] has been analyzed as discussed in Section IV and the efficiency η_d has been evaluated. Fig. 15 shows a good agreement between the curves, thus providing a solid characterization of the power meter and, moreover, a further validation of the electromagnetic model of the channel proposed in this work.

REFERENCES

[1] D. H. Auston, K. P. Cheung, and P. R. Smith, "Picosecond photoconducting Hertzian dipoles," *Appl. Phys. Lett.*, vol. 45, no. 3, pp. 284–286, Aug. 1984.

[2] P. R. Smith, D. H. Auston, and M. C. Nuss, "Subpicosecond photoconducting dipole antennas," *IEEE J. Quantum Electron.*, vol. 24, no. 2, pp. 255–260, Feb. 1988.

[3] D. R. Dykaar, B. I. Greene, J. F. Federici, A. F. J. Levi, L. N. Pfeiffer, and R. F. Kopf, "Log-periodic antennas for pulsed terahertz radiation," *Appl. Phys. Lett.*, vol. 59, no. 3, pp. 262–264, Jul. 1991.

[4] J. T. Darrow, X. C. Zhang, D. H. Auston, and J. D. Morse, "Saturation properties of large-aperture photoconducting antennas," *IEEE J. Quantum Electron.*, vol. 28, no. 6, pp. 1607–1616, Jun. 1992.

[5] M. Tani, S. Matsuura, K. Sakai, and S. Nakashima, "Emission characteristics of photoconductive antennas based on low-temperature-grown GaAs and semi-insulating GaAs," *Appl. Optics*, vol. 36, no. 30, pp. 7853–7859, Oct. 1997.

[6] A. Dreyhaupt, S. Winnerl, T. Dekorsy, and M. Helm, "High-intensity terahertz radiation from a microstructured large-area photoconductor," *Appl. Phys. Lett.*, vol. 86, no. 12, pp. 121114, Mar. 2005.

[7] S. Winnerl, F. Peter, S. Nitsche, A. Dreyhaupt, B. Zimmermann, M. Wagner, H. Schneider, M. Helm, and K. Kohler, "Generation and detection of THz radiation with scalable antennas based on GaAs substrates with different carrier lifetimes," *IEEE J. Selected Topics Quantum Electron.*, vol. 14, no. 2, pp. 449–457, Mar. 2008.

[8] S. H. Yang, M. R. Hashemi, C. W. Berry, and M. Jarrahi, "7.5% optical-to-terahertz conversion efficiency offered by photoconductive emitters with three-dimensional plasmonic contact electrodes," *IEEE Trans. THz Sci. Technol.*, vol. 4, no. 5, pp. 575–581, Sept. 2014.

[9] N. T. Yardimci, S. H. Yang, C. W. Berry, and M. Jarrahi, "High-power terahertz generation using large-area plasmonic photoconductive emitters," *IEEE Trans. THz Sci. Technol.*, vol. 5, no. 2, pp. 223–229, Mar. 2015.

[10] A. Garufo, G. Carluccio, N. Llombart, and A. Neto, "Norton equivalent circuit model for photoconductive antennas - Part I: Theoretical model," *IEEE Trans. Antennas Propag.*, submitted.

[11] QMC Instruments Ltd., Cardiff, United Kingdom.

[12] Virginia Diodes Inc., Charlottesville, Virginia, United States.

[13] Toptica Photonics AG., Munich, Germany.

[14] N. Llombart and A. Neto, "THz time-domain sensing: The antenna dispersion and a possible solution," *IEEE Trans. THz Sci. Technol.*, vol. 2, no. 4, pp. 416–423, July 2012.

[15] A. Garufo, G. Carluccio, N. Llombart, and A. Neto, "Design of photo-conductive connected arrays for pulsed terahertz radiation," *10th European Conference on Antennas and Propagation (EUCAP 2016)*, Davos, Switzerland, April 10–15, 2016.

[16] A. Garufo, N. Llombart, and A. Neto, "Radiation of logarithmic spiral antennas in the presence of dense dielectric lenses," *IEEE Trans. Antennas Propag.*, vol. 64, no. 10, pp. 4168–4177, Oct. 2016.

[17] I. S. Gregory, C. Baker, W. R. Tribe, M. J. Evans, H. E. Beere, E. H. Linfield, A. G. Davies, and M. Misssous, "High resistivity annealed low-temperature GaAs with 100 fs lifetimes," *Appl. Phys. Lett.*, vol. 83, no. 20, pp. 4199–4201, Nov. 2003.

[18] V. Ortiz, J. Nagle, J. F. Lampin, E. Peronne, and A. Alexandrou "Low-temperature-grown GaAs: Modeling of transient reflectivity experiments," *J. Appl. Phys.*, vol. 102, no. 4, pp. 043515, Aug. 2007.

[19] Tydex, St. Peterburg, Russia.

[20] Thomas Keating Instruments Ltd., Billingshurst, United Kingdom.

[21] J. Hesler, Private communication, Virginia Diodes Inc., Charlottesville, Virginia, United States, June 2016.

[22] [Online] CST Microwave Studio. Available at http://www.cst.com/.

[23] D. F. Filipovic, S. S. Gearhart, and G. M. Rebeiz, "Double-slot antennas on extended hemispherical and elliptical silicon dielectric lenses", *IEEE Trans. Microw. Theory Tech.*, vol. 41, no. 10, pp. 1738–1748, Oct. 1993.

[24] O. Yurduseven, D. Cavallo, A. Neto, G. Carluccio, and M. Albani, "Parametric analysis of extended hemispherical dielectric lenses fed by a broadband connected array of leaky-wave slots," *IET Microw. Antennas Propag.*, vol. 9, no. 7, pp. 611–617, May 2015.

[25] P. H. Bolivar, M. Brucherseifer, J. G. Rivas, R. Gonzalo, I. Ederra, A. L. Reynolds, M. Holker, and P. de Maagt, "Measurement of dielectric constant and loss tangent of high dielectric-constant materials at terahertz frequencies," *IEEE Trans. Microw. Theory Tech.*, vol. 51, no. 4, pp. 1062–1066, Apr. 2003.

[26] [Online] GRASP. Available at http:/www.ticra.com/.

[27] A. Garufo, "Towards the engineering of pulsed photoconductive antennas," Ph.D. thesis, Delft University of Technology, Delft, The Netherlands, 2017.

[28] M. C. Beard, G. M. Turner, and C. A. Schmuttenmaer, "Subpicosecond carrier dynamics in low-temperature grown GaAs as measured by time-resolved terahertz spectroscopy," *J. Appl. Phys.*, vol. 90, no. 12, pp. 5915–5923, Dec. 2001.

[29] M. C. Nuss, D. H. Auston, and F. Capasso, "Direct subpicosecond measurement of carrier mobility of photoexcited electrons in Gallium Arsenide," *Phys. Rew. Lett.*, vol. 58, no. 22, June 1987.

[30] B. Hu, X.-C. Zhang, and D. Auston, "Temperature dependence of femtosecond electromagnetic radiation from semiconductor surfaces," *Appl. Phys. Lett* vol. 57, no. 25, pp. 2629–2631, Dec. 1990.

[31] S. S. Prabhu, S. E. Ralph, M. R. Melloch, and E. S. Harmon, "Carrier dynamics of low-temperature-grown GaAs observed via THz spectroscopy," *Appl. Phys. Lett.*, vol. 70, no. 18, pp. 2419–2421, May 1997.

[32] J. T. Darrow, X. C. Zhang, D. H. Auston, and J. D. Morse, "Saturation properties of large-aperture photoconducting antennas," *IEEE J. Quantum Electron.*, vol. 28, no. 6, pp. 1607–1616, June 1992.

[33] S. Gupta, J. F. Whitaker, and G. A. Mourou, "Ultrafast carrier dynamics in III-V semiconductors grown by molecular-beam epitaxy at very low substrate temperatures," *IEEE J. Quantum Electron.*, vol. 28, no. 10, pp. 2464–2472, Oct. 1992.

[34] D. C. Look, D. C. Walters, G. D. Robinson, J. R. Sizelove, M. G. Mier, and C. E. Stutz, "Annealing dynamics of molecular-beam epitaxial GaAs grown at 200° C," *J. Appl. Phys.*, vol. 74, no. 1, pp. 306–310, July 1993.

[35] J. K. Luo, H. Thomas, D. V. Morgan, D. Westwood, R. H. Williams, and D. Theron, "Electrical characterisation of GaAs layers grown by molecular beam epitaxy at low temperature," *Inst. Phys. Conf. Ser.*, No. 141, IOP Publishing Ltd., pp. 301–306, 1995.

[36] J. Valdmanis and G. Mourou, "Subpicosecond electrooptic sampling: Principles and applications," *IEEE J. Quantum Electron.*, vol. 22, no. 1, pp. 69–78, Jan. 1986.

[37] Y. S. Lee, "Principles of Terahertz Science and Technology," vol. 170, Springer Science & Business Media, 2009.

[38] A. Deninger, Private communication, TOPTICA Photonics AG., Munich, Germany, Jul. 2016.

[39] B. Globisch, R. J. B. Dietz, T. Göbel, M. Schell, W. Bohmeyer, R. Müller, and A. Steiger, "Absolute terahertz power measurements of a time-domain spectroscopy system," *Opt. Lett.*, vol. 40, no. 15, pp. 3544–3547, Aug. 2015.

[40] D. Stanze, A. Deninger, A. Roggenbuck, S. Schindler, M. Schlak, B. Sartorius, "Compact CW terahertz spectrometer pumped at $1.5\,\mu\mathrm{m}$ wavelength," *Journal of Infrared, Millimeter, and Terahertz Waves*, vol. 32, no. 2, pp. 225–232, Aug. 2011.

Alessandro Garufo (S'13–M'17) received the B.Sc. and M.Sc. degree in telecommunication engineering from University of Siena, Siena, Italy, in 2007 and 2012, respectively, and the Ph.D. degree in electromagnetism from Delft University of Technology, Delft, The Netherlands, in 2017.

From 2011 until 2012, he was as intern in the Antenna Group at Thales Alenia Space, Rome, Italy, where he developed his M.Sc. degree thesis. In 2012, he was a researcher in the Applied Electromagnetic Laboratory (LEA) at the University of Siena, Siena, Italy. From 2013 until 2014, he was a visiting scholar in the Metamaterials and Plasmonics Research Laboratory at University of Texas at Austin, Austin, Texas, United States of America. From 2017, he is currently a Post-Doctoral Researcher at the THz Sensing Group in the Microelectronics department of Delft University of Technology, Delft, The Netherlands.

His research interest includes analysis and design of antennas, dielectric lens antennas and antenna arrays with emphasis at THz frequencies based on photoconductive sources.

Giorgio Carluccio was born in 1979 and grew up in Ortelle, Lecce, Italy. He received the Laurea degree in telecommunications engineering and the Ph.D. degree in information engineering from the University of Siena, Siena, Italy, in 2006 and 2010, respectively.

From October 2008 to March 2009 he was an Invited Visiting Scholar with the ElectroScience Laboratory, Department of Electrical and Computer Engineering, at The Ohio State University, Columbus, Ohio, USA. From February 2010 to January 2012 and from July 2013 to July 2014, he was a Postdoctoral Research Associate with the Department of Information Engineering and Mathematics at the University of Siena. From April 2012 to March 2013, he was a Postdoctoral Research Associate with the Department of Electronics and Telecommunication at the University of Firenze, Firenze, Italy. During 2012 and 2013 he also spent some months as a visiting Post-Doc Researcher with the Department of Microelectronics at the Delft University of Technology (TU Delft), Delft, The Netherlands. Since September 2014 he has been a Post-Doc Researcher with the Department of Microelectronics at TU Delft.

His research interests deal with electromagnetic wave theory, mainly focused on asymptotic high-frequency techniques for electromagnetic scattering and propagation. He also worked on the modeling and design of dielectric lens antennas, reflectarray antennas, and THz antennas based on photoconductive materials.

Joshua R. Freeman received...

David R. Bacon received...

Nuria Llombart (S'06–M'07–SM'13) received the Electrical Engineering and Ph.D. degrees from the Polytechnic University of Valencia, Spain, in 2002 and 2006, respectively.

During her Master's degree studies she spent one year at the Friedrich-Alexander University of Erlangen-Nuremberg, Germany, and worked at the Fraunhofer Institute for Integrated Circuits, Erlangen, Germany. From 2002 until 2007, she was with the Antenna Group, TNO Defence, Security and Safety Institute, The Hague, The Netherlands, working as a Ph.D. student and afterwards as a Researcher. From 2007 until 2010, she was a Postdoctoral Fellow at the California Institute of Technology, working for the Sub millimeter Wave Advance Technology Group, Jet Propulsion Laboratory, Pasadena, USA. She was a Ramn y Cajal Fellow at the Optics Department of the Complutense University of Madrid, Spain, from 2010 to 2012. In September 2012, she joined the THz Sensing Group at Delft University of Technology, Delft, The Netherlands, where she is currently an Associate Professor.

She has co-authored over 150 journal and international conference contributions. Her research interests include the analysis and design of planar antennas, periodic structures, reflector antennas, lens antennas, and waveguide structures, with emphasis in the THz range. Dr. Llombart was co-recipient of the H.A. Wheeler Award for the Best Applications Paper of the year 2008 in the IEEE Transactions on Antennas and Propagation and the 2014 Best Paper Award in the IEEE Transaction on THz Science and Technology and several NASA awards. She also received the 2014 IEEE Antenna and Propagation Society Lot Shafai Mid-Career Distinguished Achievement Award. She served as Associate Editor of the IEEE Letters on Antennas and Propagation and the IEEE Antennas and Propagation Magazine, she also served as Topical Editor of the IEEE Transaction on Terahertz Science and Technology. She serves as a Board Member of the IRMMW-THz International Society. In 2015, she was awarded with an European Research Council (ERC) Starting Grant.

Edmund H. Linfield received...

Alexander G. Davies received...

Andrea Neto (M'00–SM'10–F'16) received the Laurea degree (*summa cum laude*) in electronic engineering from the University of Florence, Florence, Italy, in 1994, and the Ph.D. degree in electromagnetics from the University of Siena, Siena, Italy, in 2000. Part of his Ph.D. degree was developed at the European Space Agency Research and Technology Center, Noordwijk, The Netherlands, where he was involved in the antenna section for over two years.

From 2000 to 2001, he was a Post-Doctoral Researcher with the California Institute of Technology, Pasadena, CA, USA, where he was involved in the Sub-Millimeter-Wave Advanced Technology Group. From 2002 to 2010, he was a Senior Antenna Scientist at TNO Defence, Security, and Safety, The Hague, The Netherlands. In 2010, he was appointed Full Professor of Applied Electromagnetism in the Electrical Engineering, Mathematics and Computer Science Faculty of Delft University of Technology, Delft, The Netherlands, where he formed and leads the THz Sensing Group. His current research interests are in the analysis and design of antennas, with emphasis on arrays, dielectric lens antennas, wideband antennas, electromagnetic band-gap structures, and terahertz antennas.

Dr. Neto was a co-recipient of the H. A. Wheeler Award for the best applications paper of the year 2008 in the IEEE Transactions on Antennas and Propagation, the Best Innovative Paper Prize at the 30th ESA Antenna Workshop in 2008, the Best Antenna Theory Paper Prize at the European Conference on Antennas and Propagation in 2010. In 2011, he was awarded the European Research Council Starting Grant to perform research on Advanced Antenna Architectures for THz Sensing Systems. He is member of the Technical Board of the European School of Antennas and organizer of the course on Antenna Imaging Techniques. He is a member of the steering committee of the network of excellence NEWFOCUS, dedicated to focusing techniques in mm and sub-millimeter-wave regimes. He was the Awards and Grants Chair of the European Conference on Antennas and Propagation in 2014. He served as an Associate Editor of the IEEE Transactions on Antennas and Propagation from 2008 to 2013, and the IEEE Antennas and Wireless Propagation Letters from 2005 to 2013. He serves as an Associate Editor of the IEEE Transactions on Terahertz Science and Technology.